Solution Structure and Backbone Dynamics of the Cysteine 103 to Serine Mutant of the N-Terminal Domain of DsbD from *Neisseria meningitides*[†,‡]

Marc Quinternet,[§] Pascale Tsan,[§] Laure Selme,[||] Chrystel Beaufils,[§] Christophe Jacob,[||] Sandrine Boschi-Muller,[||] Marie-Christine Averlant-Petit,[§] Guy Branlant,*[,||] and Manh-Thong Cung*[,§]

Laboratoire de Chimie Physique Macromoléculaire, UMR 7568 CNRS-INPL, Nancy Université, 1 rue Grandville, B.P. 20451, 54001 Nancy cedex, France, and Maturation des ARN et Enzymologie Moléculaire, UMR 7567 CNRS-UHP, Nancy Université, Faculté des Sciences et Techniques, Bld des Aiguillettes, B.P. 239, 54506 Vandœuvre-lès-Nancy, France

ABSTRACT: The DsbD protein is essential for electron transfer from the cytoplasm to the periplasm of Gram-negative bacteria. Its N-terminal domain dispatches electrons coming from cytoplasmic thioredoxin (Trx), *via* its central transmembrane and C-terminal domains, to its periplasmic partners: DsbC, DsbE/CcmG, and DsbG. Previous structural studies described the latter proteins as Trx-like folds possessing a characteristic C-X-X-C motif able to generate a disulfide bond upon oxidation. The *Escherichia coli* nDsbD displays an immunoglobulin-like fold in which two cysteine residues (Cys103 and Cys109) allow a disulfide bond exchange with its biological partners. We have determined the structure in solution and the backbone dynamics of the C103S mutant of the N-terminal domain of DsbD from *Neisseria meningitidis*. Our results highlight significant structural changes concerning the β-sheets and the local topology of the active site compared with the oxidized form of the *E. coli* nDsbD. The structure reveals a "cap loop" covering the active site, similar to the oxidized *E. coli* nDsbD X-ray structure. However, regions featuring enhanced mobility were observed both near to and distant from the active site, revealing a capacity of structural adjustments in the active site and in putative interaction areas with nDsbD biological partners. Results are discussed in terms of functional consequences.

The DsbD[1] protein is a transmembrane transporter of two electrons from the cytoplasm to the periplasm of Gram-negative bacteria such as *Escherichia coli*. DsbD is composed of three domains, all possessing two essential cysteine residues: the C- and the N-terminal domains (cDsbD and nDsbD) lie in the periplasm, whereas the third central transmembrane domain (tDsbD) is embedded in the inner membrane (*1–6*). The mechanism by which the electrons are transferred is composed of three steps involving each of the three domains: electrons are first transferred (i) from the cytoplasmic thioredoxin (Trx) to tDsbD, (ii) then from tDsbD to cDsbD, and (iii) finally from cDsbD to nDsbD (*7–11*). The nDsbD directs the electron flow either toward the cytochrome *c* biogenesis pathway, *via* the protein DsbE/CcmG, or toward the protein DsbC involved in the disulfide isomerization and in the chaperoning system (*12–14*). Moreover, it has been shown that *E. coli* nDsbD could also interact with the protein DsbG the function of which is unknown so far (*15*). All the electron transfers are mediated through disulfide bond protein exchanges between reduced and oxidized forms.

A few years ago, the structure of the oxidized form of the *E. coli* nDsbD was determined by X-ray crystallography (*4*). It displays a particular hydrophobic active site in which active cysteines (Cys103 and Cys109) are covered by a "cap loop" region (residues Asp68–Gly72) that protects them from the environment and blocks the active site from accessibility. Therefore, a structural displacement of the cap from the active site has to occur prior to reduction of the disulfide of nDsbD by cDsbD (*16*). An X-ray structural study of the mixed disulfide complex between these two partners has permitted insight to the opening of the cap concomitant to a significant repositioning of Phe70. Further, the inspection of X-ray structures of other mixed disulfide complexes involving, on one hand, *E. coli* nDsbD and, on the other hand, downstream partners DsbE/CcmG or DsbC has also shown the opening of the cap and the changeover of Phe70

(*17*). No 3D structure of the reduced form of the nDsbD has been described so far. Moreover, all of the structures of *E. coli* nDsbD (i.e, the oxidized form and the structures in covalent complexes with its biological partners) were determined by X-ray technique, which does not allow characterization of internal motions of a protein.

Recently, it has been shown that *E. coli* nDsbD is able to reduce *in vitro* the oxidized form of the N-terminal domain of PilB from *Neisseria gonorrhoeae*, which belongs to the DsbE structural family (*18*). Furthermore, in addition to these qualitative data, nDsbD from *Neisseria meningitidis* was recently isolated by our group and was shown to efficiently reduce the N-terminal domain of PilB from *Neisseria meningitidis* (k_2 value of 6.3×10^5 M$^{-1}\cdot$s^{-1}, unpublished results).

In the present work, we have resolved the 3D structure in solution and backbone dynamics of the reduced form of nDsbD from *Neisseria meningitidis* using NMR spectroscopy. In fact, it is the C103S nDsbD (nDsbD$_{C103S}$), which has been studied with the subsequent objective to characterize the dynamic and structural factors involved in molecular recognition with biological partners. The structural and dynamic properties of nDsbD$_{C103S}$ are discussed, especially for the active site and regions putatively involved in interaction, in terms of functional consequences.

MATERIALS AND METHODS

Sample Preparation. The *E. coli* strain used for nDsbD$_{C103S}$ ($\Delta 19-146$) production was C41(DE3) transformed with pETnDsbDC103S plasmid. The corresponding nDsbD fragment was obtained by PCR from *dsbD* ORF (sequences of oligonucleotides not shown), using *N. meningitidis* 8013 genomic DNA, kindly provided by Pr. Nassif (INSERM U570, Paris) between the *Nde*I and the *Sac*I sites of the pET20b plasmid. ^{15}N/^{13}C- labeled sample was prepared by growing cells in a minimal media with ^{15}NH$_4$Cl as the sole nitrogen source and with ^{13}C-labeled glucose as the only carbon source. The nDsbD$_{C103S}$ production was induced at an OD$_{600}$ of 0.6 by addition of 1 mM IPTG and harvested after 16 h for the ^{15}N/^{13}C protein by centrifugation, resuspended in minimal volume of buffer A (50 mM Tris-HCl, 2 mM EDTA, pH 8.0) with 20 mM DTT, and sonicated. After fractionated precipitation at 40% and 70% ammonium sulfate saturation in buffer A, the contaminating proteins were removed by exclusion size chromatography on ACA54 gel (IBF) equilibrated with buffer A. Purified fractions were then pooled and successively applied to a Q-Sepharose column equilibrated with buffer A, followed by a linear gradient from 0 to 0.4 M KCl (nDsbD$_{C103S}$ was eluted at 100 mM KCl) and a Phenyl-Sepharose column equilibrated with buffer A containing 1 M (NH$_4$)$_2$SO$_4$, followed by a linear gradient from 1 to 0 M (NH$_4$)$_2$SO$_4$ in buffer A (nDsbD$_{C103S}$ was eluted at 700 mM (NH$_4$)$_2$SO$_4$) connected to a fast protein liquid chromatography system (Amersham Biosciences). The sample purity and molecular mass were checked by SDS−PAGE and electrospray mass spectrometry, respectively. The protein was isolated by gel filtration on Econo-Pac 10 DG Column (Bio-Rad laboratory) equilibrated with 20 mM phosphate buffer, pH 7.0. The NMR sample contained 0.5 mM ^{15}N/^{13}C protein concentration (90% H$_2$O, 10% D$_2$O) in 20 mM phosphate buffer at pH 7.0.

NMR Spectroscopy. All spectra were acquired at 298 K on a Bruker DRX 600 MHz spectrometer equipped with a TCI cryoprobe. Spectra were processed using the program XWINNMR (Bruker) and analyzed with the program CARA (*19*). TSP-d_4 (Euriso-top) was used as an internal reference for ^{1}H chemical shift, whereas indirect referencing was used for ^{13}C and ^{15}N chemical shifts (*20*). Backbone amide ^{1}HN, ^{15}N, ^{13}C$^{\alpha}$, ^{1}H$^{\alpha}$, and ^{13}C′ and side-chain ^{1}H and ^{13}C resonances were assigned using ^{1}H−^{15}N HSQC, HNCO, HN(CA)CO, HNCA, HN(CO)CA, HNCACB, CBCA(CO)NH, and HNHA experiments. HNHB, HCCH-TOCSY, CC(CO)NH, and ^{1}H−^{15}N,^{1}H−^{13}C HSQC−NOESY spectra at two different mixing times (70 and 100 ms) were also performed for side-chain assignments. The slow amide proton exchange in D$_2$O solution (*21*) and temperature-dependence at five different temperatures (287, 291, 296, 298 and 305 K) (*22*) and the long-range HNCO experiment were used to determine the hydrogen-bond pattern of the protein (*23*).

Structure Calculations. Interproton distance restraints were derived from two-dimensional ^{1}H/^{15}N NOESY experiment and three-dimensional ^{1}H−^{13}C/^{15}N HSQC−NOESY experiments. First, ATNOS/CANDID program was used to obtain, after seven cycles, an initial set of restraints (*24, 25*). Second, the NOE cross-peak assignments and intensities were checked visually, and the restraint set was refined. Restraints for the pseudoatoms were systematically overestimated. The occurrence of a hydrogen bond was defined as a couple of distance restraints with an upper limit of 2.0 Å (up to 2.4 Å in few cases) between the acceptor heavy atom and the hydrogen atom and an upper limit of 3.0 Å (up to 3.3 Å in a few cases) between the acceptor and donor heavy atoms. Torsion restraints for the Φ and Ψ angles were derived from the program TALOS (*26*), and all the peptide bonds were kept planar and *trans*.

A total of 1500 randomized structures were calculated, and a simulated annealing process was performed using the program CYANA (*27*). The 20 structures with the lowest target function were selected and refined using DISCOVER (Accelrys Inc., San Diego, CA). Figures were drawn with the program MOLMOL (*28*).

^{15}N Relaxation Experiments. The ^{15}N longitudinal relaxation rate (R_1), ^{15}N transverse relaxation rate (R_2), and steady-state {^{1}H}−^{15}N heteronuclear NOE experiments were recorded at 298 K on a Bruker 600 MHz spectrometer, using the usual pulse sequences (*29*). A total of 256 (^{15}N) and 2048 (^{1}H) complex points were collected for the R_1 and R_2 experiments, with eight transients per increment and a recycle delay of 5 s. Ten inversion recovery delays of 2, 50, 100, 200, 300, 400, 600, 800, 1000, and 1200 ms were used for R_1 measurement, whereas eight delays of 8, 16, 32, 48, 64, 80, 112, and 144 ms were used during the CPMG (Carr−Purcell−Meiboom−Gill) period of the R_2 experiments. {^{1}H}−^{15}N NOE spectra were recorded in an interleaved way with and without proton saturation during relaxation delay, using 256×2 (^{15}N) and 2048 (^{1}H) complex points and 56 transients per increment typically. The ^{1}H saturation was achieved by the application of 120° ^{1}H pulses separated by 5 ms for a period of 4 s. Spectral widths for all heteronuclear experiments were 2433 Hz (^{15}N) and 8389 Hz (^{1}H) with carrier frequencies at 117.6 and 4.70 ppm, respectively. Data were processed using XWINNMR (Bruk-
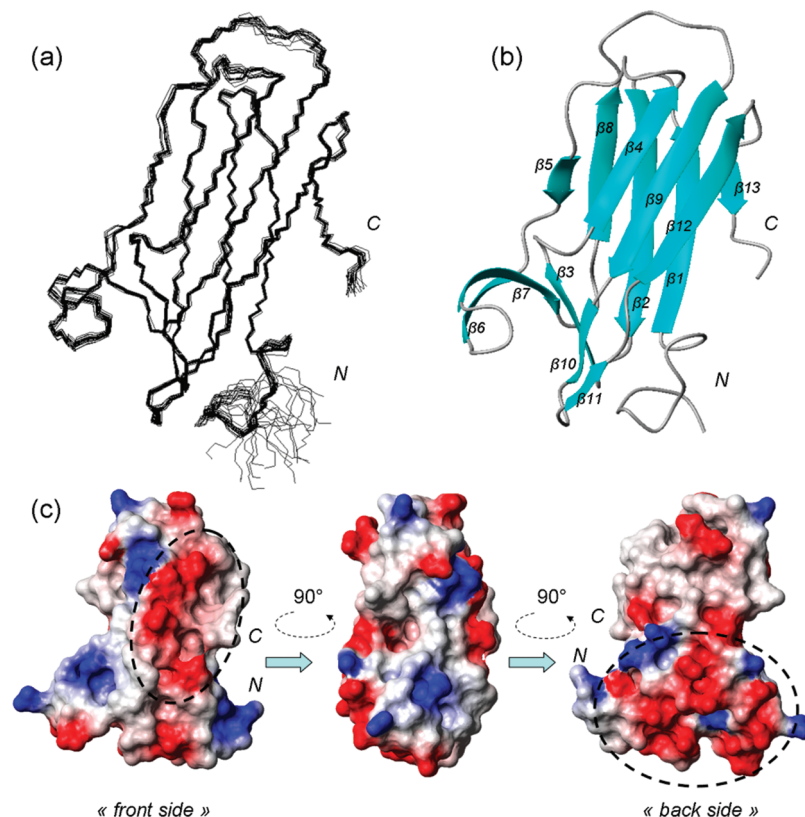
FIGURE 1: Solution structure of nDsbD$_{C103S}$: (a) backbone superimpositions from Asn9 to Tyr125 are shown for the 20 representative structures; (b) the different secondary structure elements are figured on the mean structure; (c) the electrostatic potential is represented on three different spatial orientations of nDsbD$_{C103S}$ NMR mean structure using blue (for positive potential), red (for negative potential), and white (for neutral potential) color graduations.

er). They were zero-filled in the ^{15}N dimension and apodized with a shifted square sine-bell window in both dimensions.

Backbone Dynamics Analysis. NMRVIEW software (*30*), version 6.6.2, was used to measure the peak heights of the ^{15}N$-^{1}$H cross-peaks and to determine the R_1 and R_2 values from a fit to a single-exponential decay function and also the $\{^{1}$H$\}-^{15}$N heteronuclear NOE from the ratio between the intensities of a peak in the spectra collected with and without proton saturation. All experiments were performed twice to provide an estimation of the uncertainty on R_1, R_2, and NOE values.

R_1, R_2, and NOE relaxation parameters were analyzed by means of reduced spectral density mapping at $J_{eff}(0)$, $J(\omega_N)$, and $\langle J(\omega_H)\rangle$ values (*31*–*34*) using a chemical shift anisotropy of -160 ppm for the backbone amide group (*35*) and a NH bond length of 1.02 Å. $J_{eff}(0)$ denotes that the exchange contribution to R_2 is not explicitly considered (*36*). $\langle J(\omega_H)\rangle$ is the average of $J(\omega_H)$, $J(\omega_H + \omega_N)$, and $J(\omega_H - \omega_N)$, which can be approximated by $J(0.87\omega_H)$ (*31*). Tensor2 (*37*) was used for the Lipari–Szabo analysis (*38, 39*) of the backbone ^{15}N relaxation parameters. Only residues in secondary structure elements were used for determination of the overall tumbling.

RESULTS

Structure Calculations of nDsbD$_{C103S}$. nDsbD$_{C103S}$ has been studied in a soluble state ranging from Met4 to Thr129, the numbering following that of the N-terminal domain of DsbD from *E. coli*. The chemical shift assignments have been previously reported (*40*). A nearly complete assignment of

the backbone and of the side chains has been realized except for Ala5, Leu6, Pro13, and Pro111. Superimposition of ^{1}H$-^{15}$N HSQC spectra of the C103S mutant with the wild-type *N. meningitidis* nDsbD does not display major chemical shift variations of backbone amide groups, except for some residues in the vicinity of S103; this observation suggests that the mutant and wild-type proteins exhibit the same structural features (see Supporting Information, Figure S1). Moreover, no significant chemical shift perturbation is observed for C$^{\alpha}$ and C$^{\beta}$ atoms of all the residues, except of course, for the residue 103 (data not shown).

The NMR solution structure of nDsbD$_{C103S}$ was calculated using NOE-derived restraints, backbone dihedral angle restraints derived from TALOS prediction (*26*), and hydrogen bond restraints obtained from the long-range HNCO experiment (*23*). The superimposition of the 20 representative structures for nDsbD$_{C103S}$ is shown in Figure 1a, and the structural statistics are summarized in Table 1. Only two restraint violations greater than 0.3 Å have been observed. According to PROCHECK-NMR analysis (*41*), 79.0% of the nonglycine and the nonproline residues remain in the most favored regions of the Ramachandran plot, whereas 15.2% and 4.8% of the whole residues are, respectively, in the additionally allowed and generously allowed regions. Only 1% of the residues (Lys62) is located in disallowed regions. Moreover, the fine packing quality control analysis, performed with WHAT IF (*42*) using the most representative structure of nDsbD$_{C103S}$, identifies this structure as a good one (WHAT IF Z-score for all contacts of -1.34). Considering the sequence from Asn9 up to Tyr125, the final 20

Table 1: NMR-Derived Geometrical Restraints and Structural Statistics of the Entire Conformational Set of nDsbD$_{C103S}$

restraint	number
upper interproton	
total of distance restraints	2059
intra	350
short	641
medium	227
long distance	751
H-bonds[a]	90
dihedral angle	154
ϕ	66
ψ	69

violation	occurrence
distance violation >0.3 Å	2
dihedral violation >5°	0

Ramachandran statistics (PROCHECK-NMR)	
residues in the most favorable region (%)	79.0
residues in additionally allowed regions (%)	15.2
residues in generously allowed regions (%)	4.8
residues in disallowed regions (%)	1.0
Fine packing quality control (WHAT IF)[b]	
Z-score for all contacts	−1.34

atoms (residues 9−125)	rmsd (Å)
backbone	0.43 ± 0.09
heavy	1.10 ± 0.12

[a] Each hydrogen bond is treated as two distance restraints so that 45 hydrogen bonds lead to 90 distance restraints. [b] The analysis has been performed using the most representative structure of nDsbD$_{C103S}$

calculated structures exhibit an atomic rmsd from the mean structure of 0.43 ± 0.09 Å for the backbone atoms and 1.10 ± 0.12 Å for all heavy atoms. In parallel to atomic rmsd, all Φ and Ψ dihedral angles are well-defined with low standard deviations except the Met4−Leu11, Ala52−Asp53, Ser61−Glu64, and Ala88−Glu93 sequences for which significant standard deviation values are observed and are indicative of less-defined structural parts.

Structure Analysis of nDsdD$_{C103S}$. The core of the protein exhibits mainly three β-sheets, all composed of antiparallel individual strands (Figure 1b). The first β-sheet comprises five strands from Phe18 to Val24 for β1, Gly28 to Ile35 for β2, Ser59 to Phe60 for β5, Glu80 to Pro86 for β8, and Thr124 to Tyr125 for β13. The second β-sheet comprises five strands from Tyr39 to Tyr42 for β3, Glu64 to Glu67 for β6, Arg73 to Tyr77 for β7, Gly102 to Ala104 for β10 and Val108 to Cys109 for β11. The third β-sheet comprises three strands from Val47 to Asn50 for β4, Tyr94 to Tyr100 for β9, and Val113 to Ile119 for β12. All these β-strands are clearly well-defined as proven by a weak backbone rmsd value of 0.27 ± 0.07 Å on β-stranded secondary structures. According to NOE restraint data, one α-helix turn seems possible from Pro14 to Ala17. Globally, only the N-terminal region, from Met4 to Ala8, is largely disordered in all 20 NMR structures due to the partial chemical shift assignment and the lack of NOE restraints.

As investigated on DALI (*43*) and VAST (*44*) servers, the fold adopted by nDsbD$_{C103S}$ is part of the immunoglobulin superfamily. Two main features characterize the structure adopted by this protein in solution: the first and the third β-sheets are arranged in a β-sandwich, while the second

β-sheet forms a partial β-barrel. More precisely, the β-sandwich is mainly formed by strands β1, β2, and β8 on one hand and strands β4, β9, and β12 on the other hand. It is flanked by strands β5 and β13, which are, respectively, hydrogen bonded to strands β8 and β1 (Figure 1b). These hydrogen bonds were highlighted by the NMR HNCO long-range experiment. The partial β-barrel contains the active site (Figure 2a). Indeed, Ser103 (equivalent to *E. coli* Cys103) and Cys109 are, respectively, located on strands β10 and β11, and both side chains point toward the inner cavity of the partial β-barrel. More precisely, side chains of Tyr40, Tyr42, and Phe70 point toward Ser103 and Cys109, the conformation of aromatic rings being well-defined in all 20 NMR structures. Besides, the cavity of the partial β-barrel contains four aromatic side chains, thus endowing the active site with a particularly hydrophobic environment, enhanced by the side chain of Val76. Moreover, the aromatic rings of Tyr39 and Tyr110 lie on the external face of the partial β-barrel and cover the backbone atoms of Ser103 and Cys109, the residues Ala104, Ala106, and Val108 enhancing the hydrophobicity of this external face. All of these features give the inner active site a particular hydrophobic character.

The electrostatic potential of nDsbD$_{C103S}$ surface has been calculated and figured using MOLMOL (*28*). As far as the "back side" of nDsbD$_{C103S}$ (see Figure 1c for spatial orientation) is considered, it points out that potential charges are spread over the surface of strand β6 and surrounding residues. Indeed, the potential charges of Asp37 and Glu105 permit definition of a remarkable negatively charged side of the nDsbD$_{C103S}$ active site. The same phenomenon is observed on the "front side" along strand β12. In contrast, the surface of the region opposite to the active site is globally less charged.

Reduced Spectral Density Mapping and Model-Free Analysis. The ^{15}N longitudinal relaxation rate (R_1), ^{15}N transverse relaxation rate (R_2), and steady-state {^{1}H}−^{15}N heteronuclear NOE values of nDsbD$_{C103S}$ were measured for 107 backbone NH groups out of the 118 nonproline residues, (Figure 3a−c). The unanalyzed residues either were unassigned or overlapped. The average values for the backbone ^{15}N-nuclei are: $\langle R_1 \rangle = 1.51 \pm 0.04$ s^{-1}; $\langle R_2 \rangle = 9.41 \pm 0.31$ s^{-1}; $\langle NOE \rangle = 0.74 \pm 0.01$ s^{-1}. The relaxation parameters plotted versus the protein sequence globally display a nonlinear profile. For instance, a sharp drop of all three parameters is found within the N- and C-termini, around Val91, and here and there along the sequence.

Reduced spectral density mapping, which does not require any model, was used first to analyze the relaxation data. The $J_{eff}(0)$, $J(\omega_N)$, and $\langle J(\omega_H) \rangle$ obtained values are represented in Figure 3d−f. A sharp decrease of $J_{eff}(0)$ compensated for a large increase of $\langle J(\omega_H) \rangle$ observed within the N-terminus, the C-terminus, and the segment Lys89−Glu93 and for residue Gly121. This indicates the flexibility at both extremities of the protein, as well as in the β8−β9 loop and for Gly121. Residues Glu15, Gln43, Ala44, Gly63, and Val108 exhibit relatively high $J_{eff}(0)$ values, while their $J(\omega_N)$ and $\langle J(\omega_H) \rangle$ values are not lower than the average, which suggests the contribution of microsecond−millisecond time scale chemical exchange. $J(\omega_N)$ values do not vary much along the sequence, indicating proximity to the isobestic frequency, where the contribution of $J(\omega)$ is independent of the internal mobility (*46*).
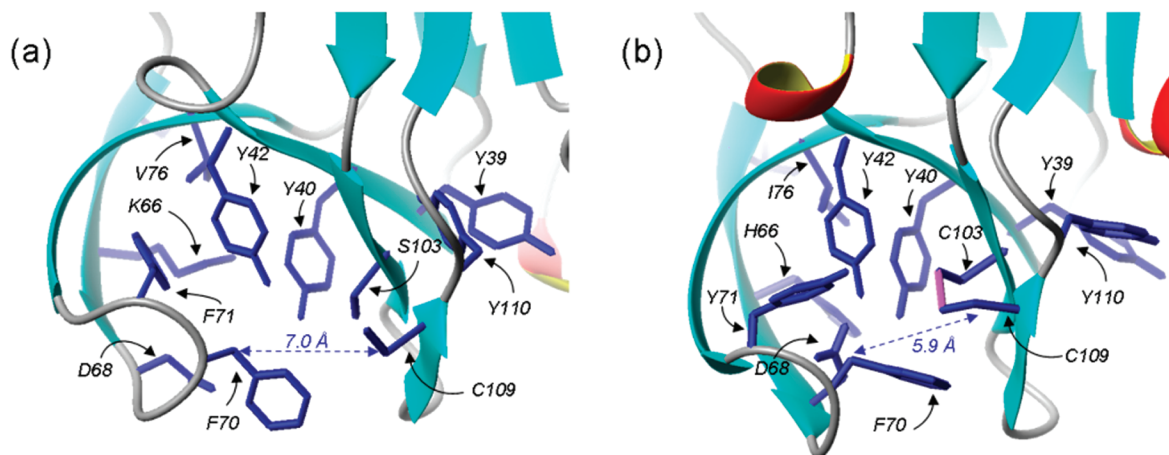
FIGURE 2: Active site of the most representative NMR solution structure of *N. meningitidis* nDsbD$_{C103S}$ (a) and X-ray oxidized structure of *E. coli* nDsbD (b). Only heavy atoms are represented for the side chains. The disulfide bond in *E. coli* nDsbD X-ray structure is figured in purple. The distance between C$^{\beta}$ atoms of residues Phe70 and Cys109 is indicated with dashed arrows.
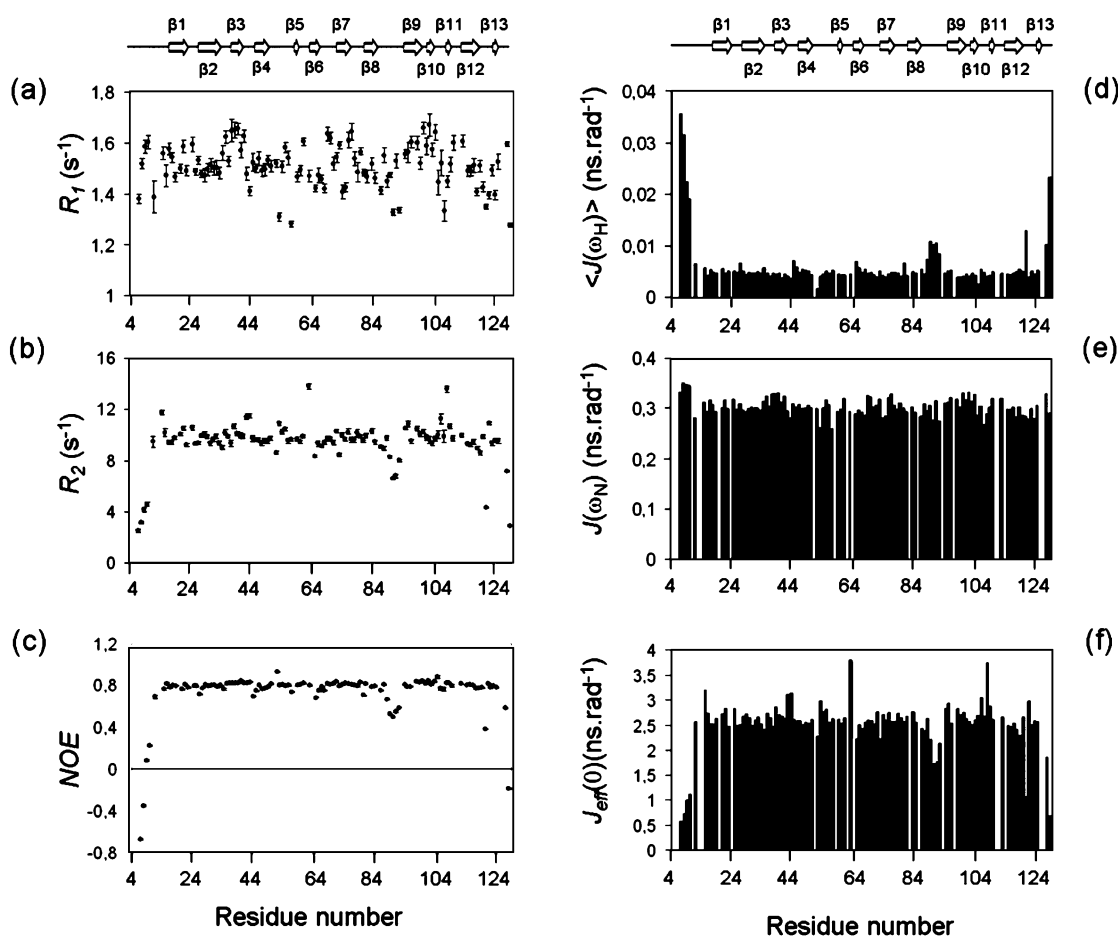

FIGURE 3: ^{15}N longitudinal relaxation rates, R_1 (a), ^{15}N transverse relaxation rates, R_2 (b), and steady-state {^{1}H}$-^{15}$N heteronuclear NOE values (c) of nDsbD$_{C103S}$ are plotted versus the amino acid sequence. Reduced spectral density functions of nDsbD$_{C103S}$, $\langle J(\omega_H)\rangle$ (d), $J(\omega_N)$ (e), and $J_{eff}(0)$ (f), are also shown. Experiments were recorded on a Bruker DRX 600 MHz at pH 7.00, 25 °C. The secondary structure elements extracted from the mean structure are shown at the top.

To get a detailed picture of the global and internal dynamics of nDsbD$_{C103S}$, the relaxation parameters were analyzed with a Lipari−Szabo approach (*38, 39*) by means of the Tensor2 software (*37*) and using the mean NMR structure. The R_2/R_1 ratios of the residues involved in secondary structures were used to determine the rotational diffusion tensor describing the overall tumbling of the protein. The principal components obtained are $D_x = 1.95 \times 10^7$, $D_y = 2.14 \times 10^7$, and $D_z = 2.57 \times 10^7$ s^{-1}, which gives a global correlation time of 7.38 ns, in agreement with a monomeric state. Besides, the direction of the principal axes, as well as the axial anisotropy ($2D_z/(D_x + D_y) = 1.26$) and the rhombicity ($D_x/D_y = 0.91$), are in agreement with the inertia tensor of the nDsbD$_{C103S}$ structure (see Figure 4).

The results for the internal mobility are represented in Figure 5. The mean and median order parameters S^2 are respectively 0.81 and 0.86. As generally observed in proteins, the N- and C-terminal extremities of nDsbD$_{C103S}$ show fast
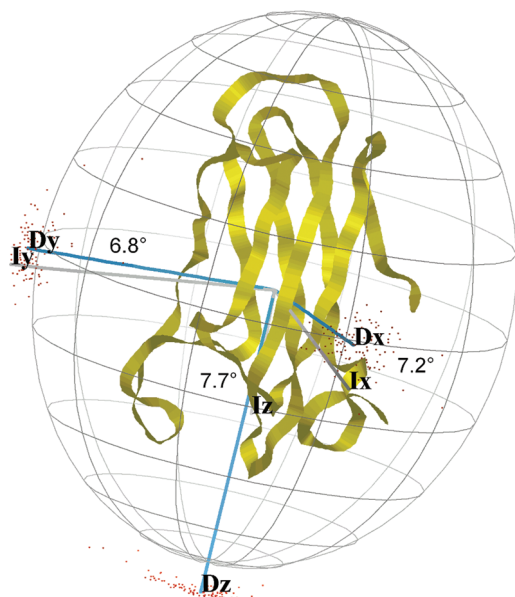
FIGURE 4: Representation of the principal axes D_x, D_y, and D_z of the diffusion tensor (blue) and of the principal axes I_x, I_y, and I_z of the inertia tensor (gray) on the nDsbD$_{C103S}$ mean structure. The dispersion of the diffusion tensor axes, as determined by 100 Monte Carlo simulations, are reported using a scatter plot. The angle values between the respective axes of the diffusion tensor and of the inertia tensor are reported, and the N- and C-terminal regions are indicated. The figure has been generated by Tensor2 (*37*).

motions of large amplitude, as depicted by weak S^2, associated here to internal correlation times $\tau_i < 0.1$ ns or $\tau_i > 0.1$ ns, and by high $\langle J(\omega_H)\rangle$ values. This can be related to the high backbone rmsd values observed in these segments (Figure 5a). Likewise, the region Ala90−Glu93, which lies at the opposite side of the active site and which is also less-defined in the NMR structure, displays similar striking dynamic features. Mobility is observed in the surrounding loops Ala25−Asp27 and Phe120−Gly123 too, as reflected by a weak S^2, the presence of τ_i or that of chemical exchange. Chemical exchange is indeed highlighted by high R_{ex} term and $J_{eff}(0)$ values for residues Phe120 and Asn122, as well as for Glu15, Gln43, Ala44, Asp53, Gln57, Gly63, Tyr94, and Val108. It can be noticed that some particular residues, located in secondary structures, display interesting dynamics parameters notably in the region of strands $\beta6$ and $\beta7$, even if their backbone rmsd is low. More precisely, Gly63, Glu65, Lys66, Glu67, Asp68, and Arg73, as well as the bend Gln43−Ile46, show particular profiles of reduced spectral density mapping and possess particular S^2, τ_i, or R_{ex} terms (deviating at least from one standard deviation around the median value calculated on residues belonging to the core of the protein).

DISCUSSION

nDsbD$_{C103S}$ Global Topology. N. meningitidis nDsbD$_{C103S}$ displays an immunoglobulin-like fold comprising first a β-sandwich and second an active site shaped as a partial β-barrel. DALI and VAST investigations list *E. coli* nDsbD as the best structural homologue to nDsbD$_{C103S}$. The amino acid sequence alignment shows that they share 26% sequence identity and that several residues surrounding the active site are conserved (Figure 6a). As expected, strong structural similarity is then observed with the oxidized *E. coli* nDsbD
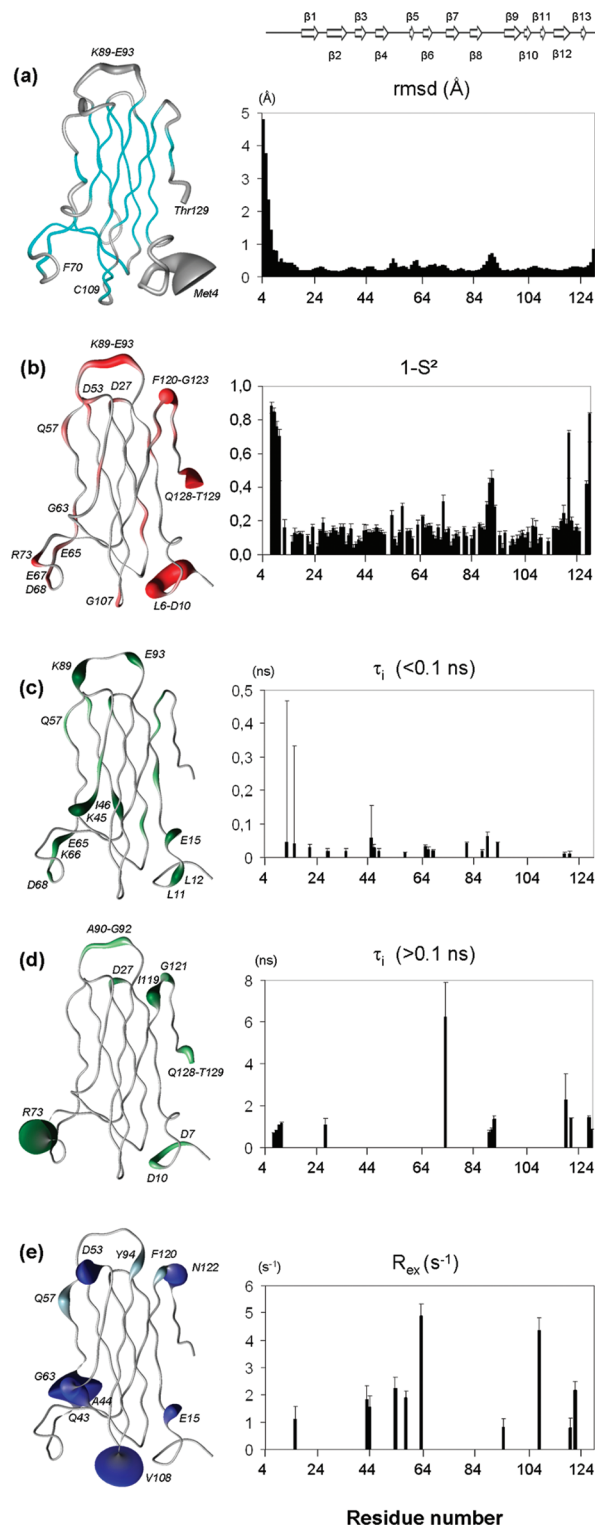

FIGURE 5: Backbone rmsd and model-free internal mobility parameters of nDsbD$_{C103S}$: (a) backbone rmsd; (b) order parameter S^2; (c) slow (>0.1 ns) and (d) fast (<0.1 ns) internal correlation time τ_i; (e) exchange term R_{ex} versus the amino acid sequence. All these parameters are plotted versus the amino-acid sequence and are also shown on the mean structure with the following rules: for panel a, the width of the spline is proportional to rmsd value and blue color is used to indicate secondary structure elements; for panels b−e, the width of the spline and the color intensity are proportional to the values on the graphical representation; for high values, the proportionality factor with the width of the spline has been decreased to avoid plot overloading. Some particular residues have been reported on the structure to facilitate the reading of the schemes. The secondary structure elements extracted from the mean structure are shown at the top.
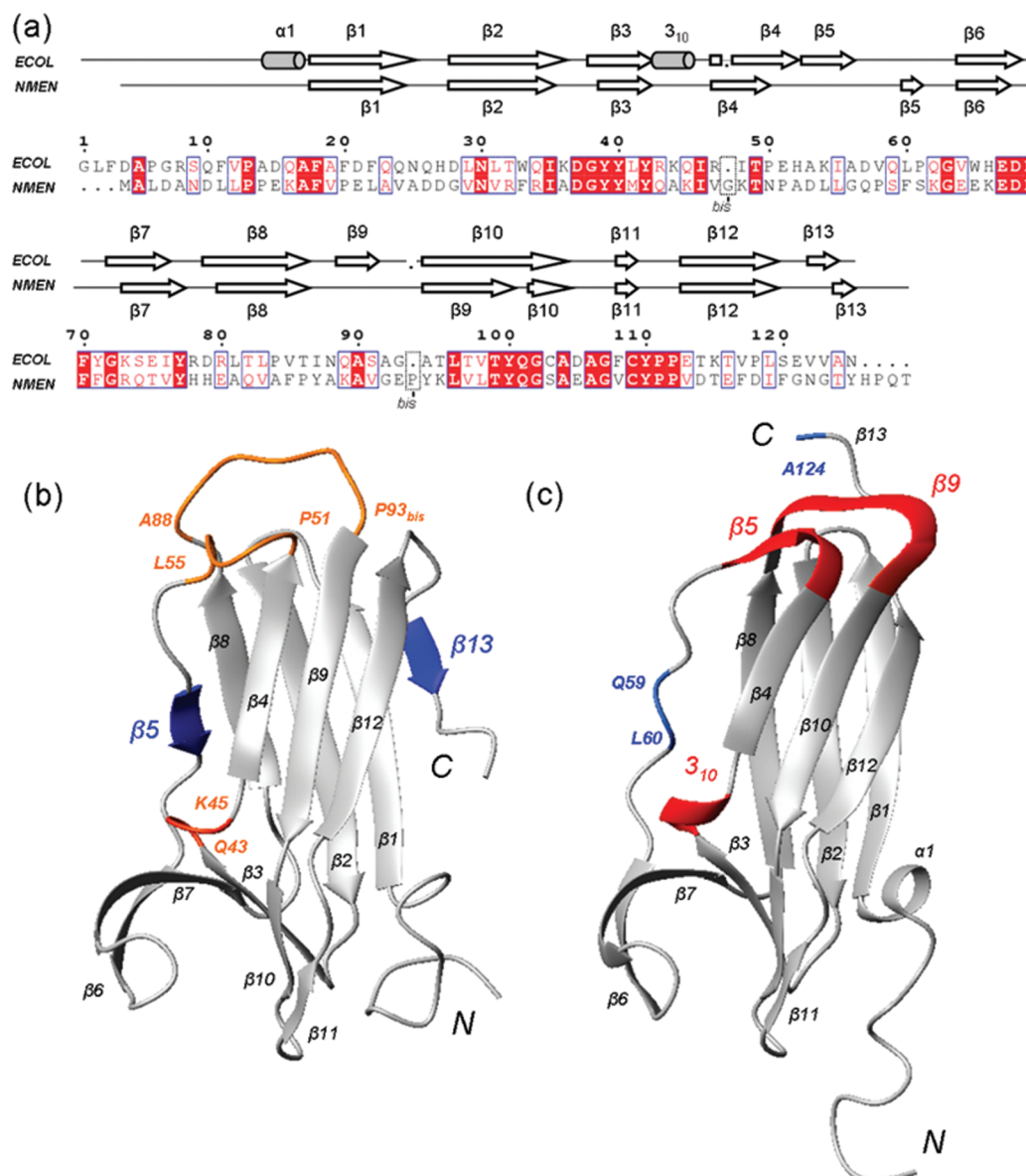
FIGURE 6: Alignment of amino acid sequence and secondary structures between *E. coli* nDsbD and *N. meningitidis* nDsbD$_{C103S}$ (a). The numbering follows that of *E. coli* nDsbD, and the two insertions have been reported as residues Gly47$_{bis}$ and Pro93$_{bis}$. The figure was prepared with help of *ESPript* (*48*). Secondary structure numbering of *E. coli* nDsbD was reported according to Goulding et al. (*4*). Comparison between nDsbD$_{C103S}$ NMR solution structure (b) and *E. coli* nDsbD X-ray structure (c). The PDB access number 1L6P was used for *E. coli* nDsbD structure. Divergent secondary structure elements are, respectively, colored in blue and red on nDsbD$_{C103S}$ and *E. coli* nDsbD structures. Absence of clear secondary structures on one or the other, structure is highlighted with clearer colors. The figures were prepared with MOLMOL using default setting for secondary structures display (*28*).

X-ray structure (PDB access code 1l6p and 1jpe) (*4*), the unique structure available for an unliganded state of this N-terminal domain. However, several differences, notably in the secondary structures, can be highlighted. First of all, obvious indications of conformational changes are highlighted by the high difference of the Φ and Ψ dihedral angle values comparing the well-defined parts of the *N. meningitidis* nDsbD$_{C103S}$ NMR structure with those of the *E. coli* nDsbD X-ray structure (Figure 7). Significant changes are observed essentially for the segments between the different strands and, also to a lesser degree, for some residues inside the β1, β8, β9, and β10 strands in nDsbD$_{C103S}$. This leads to slight untwisting of the β-sandwich in nDsbD$_{C103S}$. A few minor differences can be underlined such as the length of the strands β1, β6, and β7, one residue shorter than their equivalents in *E. coli* nDsbD. Besides, the segment Gln43−Ile46 does not form a 3$_{10}$-helix but only a bend,

which is consistent with the presence of exchange terms R_{ex} and fast τ_i in this segment, since no secondary structure is observed. More importantly, several striking changes appear clearly in the composition of the β-sheets (Figure 6b,c). First, the first β-sheet of nDsbD is made up of three β-strands (β1, β2, and β8) in *E. coli*, whereas it contains two short additional strands (β5 and β13) highlighted by long-range HNCO and 3D NOESY-HSQC experiments in *N. meningitidis*. The presence of these two strands is supported by the observation of high order parameters, similar to those found in the other rigid β-sandwich secondary structures of nDsbD$_{C103S}$. This major difference with *E. coli* nDsbD is due to the presence of hydrogen bonds in nDsbD$_{C103S}$ between Ser59-NH and Ala84-CO and Ser61-NH and Gln82-CO creating strand β5 and hydrogen bonds between Val24-NH and Gly123-CO and Leu22-NH and Tyr125-CO creating strand β13. Second, despite compatible backbone torsion
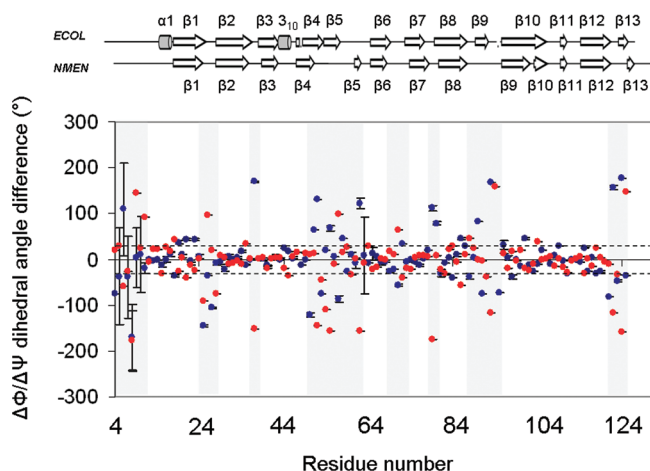
FIGURE 7: Graphical representation of the difference of Φ and Ψ dihedral angle values between the *E. coli* nDsbD X-ray structure and the *N. meningitidis* nDsbD_{C103S} NMR structure along the amino-acid sequence. The blue and the red circles represent the variation of $\Delta\Phi$ and $\Delta\Psi$, respectively. The horizontal lines at 30° and −30° delimit the regions that undergo significant Φ and Ψ dihedral angle changes. Secondary structures of the *E. coli* and *N. meningitidis* nDsbD structures are shown at the top.

angles, the segment Asp57−Gly63 in *E. coli* nDsbD X-ray structure does not display hydrogen bonds permitting the formation of a β-strand. In nDsbD_{C103S}, a β strand is found in this region. Third, as described by the authors, the C-terminal end of *E. coli* nDsbD is able to adopt, in the X-ray structure, a β-sheet conformation involving the *E. coli* $\beta5$, $\beta9$, and $\beta13$ strands, which places this C-terminal segment on the opposite side of the N-terminus. Here, the four-residue longer C-terminal tail of nDsbD_{C103S} is completely reoriented compared with that of *E. coli* nDsbD: it forms a strand $\beta13$ antiparallel to strand $\beta1$ and thus comes closer to the N-terminal extremity. The mobility found in the preceding loop Phe120−Gly123 may permit this strand $\beta13$ to move along strand $\beta1$ and to participate to the β-sheet. These observations, done between nDsbD_{C103S} and *E. coli* nDsbD, highlight the powerful role of NMR in revealing clear structural differences across bacterial species or oxidation states.

The Active Site: A Hydrophobic Cavity Covered by a Cap Loop. As it has been observed for the oxidized *E. coli* nDsbD structure, the nDsbD_{C103S} active site contains a highly hydrophobic cavity with several aromatic residues. Likewise, the two strands $\beta6$ and $\beta7$ cover Ser103 and Cys109. The cleft of the partial β-barrel is thus cluttered with long side chains and access for substrates to active residues is consequently restricted. Interestingly, the so-called "cap loop" situated between strands $\beta6$ and $\beta7$ and more particularly the Phe70 side chain close the entrance to this cavity, like in the oxidized *E. coli* nDsbD. Therefore, the cap loop adopts a "closed position" and should possess a protective role in the reduced state too. Nevertheless, even if most of the residues forming the structure of the partial β-barrel in *E. coli* nDsbD are conserved in nDsbD_{C103S}, notably those whose side chains point toward the internal cavity, significant changes occur because of a single amino acid substitution at position 71 in the active site. Indeed, the aromatic ring of Phe71 from nDsbD_{C103S} is largely reoriented compared with its equivalent Tyr71 in *E. coli* nDsbD, which is less hydrophobic and points toward the solvent (Figure 2a,b). The

major consequence is to enlarge the internal diameter of the cavity. In nDsbD_{C103S}, the aromatic ring of Phe71 interacts in a parallel manner with that of Tyr42, interacting itself with Tyr40 and Ser103. To avoid steric congestions, this network of interactions forces the cleft of the partial β-barrel to be larger. In *E. coli* nDsbD, the aromatic ring of Tyr42 interacts with Tyr40 and Cys103 but orthogonally to that of Tyr71. The steric constraints are consequently weaker inside the cavity. That is the reason that the aromatic ring of Phe70 can move closer to Cys109, thus involving a tightening of the partial β-barrel, as depicted by the decrease of distance from 7.0 to 5.9 Å between the C^β atoms of Phe70 and Cys109 compared with their equivalent residues in nDsbD_{C103S} (see Figure 2).

Role of Asp68. It had been proposed that the Tyr42 residue from *E. coli* nDsbD could mediate, instead of a water molecule, the proton transfer between Asp68 and Cys103 residues, thanks to close distances between the hydroxyl, carboxyl, and thiol groups of the latter residues (*4*). In the bunch of nDsbD_{C103S} NMR structures, the mean distance between the O$^\gamma$ from Tyr42 residue and the O$^\gamma$ from Ser103 residue is equal to 4.16 ± 0.21 Å. This is comparable to the distance of 3.51 Å found for the equivalent residues in *E. coli* oxidized nDsbD and compatible with the hypothesis raised by Goulding et al. (*4*), However a mean distance of 6.48 ± 0.66 Å is observed between the O$^\gamma$ from Tyr42 residue and the carboxyl group of Asp68 residue in nDsbD_{C103S}, whereas the corresponding atoms in *E. coli* nDsbD are separated by only 2.69 Å. Moreover it seems that these two residues do not display the sufficient dynamic properties to come closer. In regards to all these structural features, it is likely that the proton transfer between Asp68 and Cys103 residues in the native nDsbD from *Neisseria* genus may be orchestrated by an additional element, even if the Tyr42 residue is involved.

Dynamics in the Active Site. Dynamic properties of the active site have been analyzed more particularly in order to get insight into the enzymatic mechanism. Flexibility of the partial β-barrel should be considered as a prerequisite in the enzymatic scheme so as to cross the barrier of steric congestions inside the cavity. It has been suggested that the better reactivity of Cys109 compared with Cys103 in *E. coli* nDsbD was due to steric congestion around Cys103 (*4*). About this hypothesis, a large but isolated exchange term, R_{ex}, has been found for the Val108 residue neighboring Cys109 in nDsbD_{C103S}. However, its particular dynamic features could denote that this term may mainly reflect motions of aromatic side chains in the neighborhood of the Val108 NH group (*45*), rather than backbone conformational changes that could facilitate access to solvent. Indeed, as other residues exhibiting a significant R_{ex} term, the HN group of Val108 is close to aromatic rings, notably to that of Phe70 (and may therefore be sensitive to the variations of the ring-current effects induced by their motions). Nonetheless, it is reasonable to assume that conformational exchange can have a contribution, even minor, to all these exchange terms thus conferring some mobility to the backbone of nDsbD_{C103S}, as depicted for example by the slight decrease of S^2 term for Val108.

Since structural changes have to make the catalytic cysteine accessible to substrate and since most of the residues surrounding sequentially Cys109 do not display sufficient

mobility to expose it, it is likely that the cap loop region of nDsbD$_{C103S}$ displays a particular dynamics profile. Actually, our dynamics study highlights significant motions, notably for Gly63, Glu65, Lys66, Glu67, Asp68, and Arg73, indicating the ability for the backbone to be flexible in the segment around Phe70 residue of nDsbD$_{C103S}$ and therefore to adapt its conformation to the disulfide oxido-reduction partner. Consistently, the absence of motions for Phe70 in *N. meningitidis* nDsbD$_{C103S}$ is in agreement with its protection role against nonspecific interactions with cysteine residues. The motions observed at the beginning of strand $\beta6$ suggest that the Gly63−Glu65 segment could act as a hinge permitting the opening of the partial β-barrel and recognition of the substrates. Likewise, mobility of the Gln43−Ile46 bend could reinforce this idea by introducing potential backbone adaptability near strands $\beta6$ and $\beta7$. This could explain the rearrangement observed upon complex formation in the *E. coli* nDsbD equivalent His66−Ser74 segment including Phe70 (*47*). Indeed, (while the position of the segment including Cys109 is hardly altered) the Asp68−Gly72 "cap loop" region acting as a closed gate is opened up as shown in the X-ray structure of the complexes with the upstream cDsbD (*16*) or the downstream DsbC (*5*) and CcmG (*17*).

Finally, we have shown that the cap loop adopts a "closed gate position" in the structure of nDsbD$_{C103S}$ presenting a reduced form similar to that in the oxidized *E. coli* nDsbD. This involves that the recognition of the nDsbD reduced or oxidized forms by its partners would not rely on the cap loop conformation itself but rather on specific dynamic properties or on other structural elements. Moreover, it shows that the active cysteines are covered by this loop in both redox states, which confers to this loop a protective role, a requirement to avoid the nDsbD interacting nonspecifically. This implies that an opening of the cap must occur upon formation of a complex between nDsbD and its protein partner, in which the catalytic cysteine and the recycling one would become accessible to a reagent. The "opening of the gate" necessitates a conformational change, which could be allowed thanks to the significant motions identified in the Gly63−Arg73 segment and for the Gln43−Ile46 bend, which should consequently be observed in the oxidized form too.

Indeed, in *E. coli* oxidized nDsbD, the S−π interaction between Sγ atom of Cys109 and the aromatic ring of Phe70 is described as stabilizing the disulfide bond (*4*). This observation suggests that this interaction indirectly maintains the closed position of the cap loop. Considering the bunch of the 20 reduced nDsbD$_{C103S}$ structures, such S−π interaction does not exist because of an incompatible angle between the aromatic ring of Phe70 and Cys109. Yet, the cap loop is maintained closed. Therefore, the opening of the cap loop during the formation of complexes involving the reduced form of nDsbD and downstream oxidized partners CcmG (*17*) and DsbC (*5*) could not be driven by the rupture of this particular interaction but by the dynamics of the $\beta6$−$\beta7$ region. We can thus assume that the opening of the cap occurring with the formation of the complex between the oxidized form of nDsbD and the upstream reduced partner cDsbD (*16*) is also driven by dynamic properties. Even if the rupture of the S−π interaction is required, we can legitimately think that, in the absence of relaxation data

concerning the oxidized form, the active site of the oxidized nDsbD should display similar dynamics features.

The cap displacement would necessarily be triggered by the interaction with a specific biological partner. The induced conformational change would be such that the pK_a of Cys109, which is above 8.5 in the unbound state (unpublished results), is lowered. This would consequently allow a nucleophilic attack. It is therefore important to identify the recognition elements involved in nDsbD interactions to elucidate its mechanism. Other putative interaction regions in nDsbD$_{C103S}$ are then discussed hereafter.

Other Putative Interaction Sites with Biological Partners. An interesting region around strand $\beta12$ displays a large negatively charged surface, as highlighted by the electrostatic potential analysis of nDsbD$_{C103S}$ (Figure 1c). This side of the protein corresponds to the interaction area of *E. coli* nDsbD with the subunit of the dimeric DsbC that is not reduced by nDsbD, as revealed by the X-ray structure of the complex (*5*). The potential charge repartition along the structure is quite similar between *E. coli* nDsbD and nDsbD$_{C103S}$ (see Supporting Information, Figure S2), but these negatively charged patches in nDsbD$_{C103S}$ could enable many more electrostatic interactions and thus should be also involved in the recognition with DsbC (or an equivalent in the *Neisseria* genus) or other protein partners. The slight decrease of the S^2 term observed along the $\beta12$ strand could strengthen the assumption that this region may need to drive such interactions.

Another remarkable part of nDsbD$_{C103S}$ lies at the opposite side of the active site. It is assumed in *E. coli* nDsbD to be interacting with the transmembrane domain tDsbD. It is to be noticed that this local region is not as well-defined as the rest of the protein and does not show β-strands equivalent to *E. coli* $\beta5$ and $\beta9$ strands. Despite characteristic H$^\alpha_i$/H$^N_{i+1}$ NOE correlations, no hydrogen bonds and no long-distance H^N/H^N or H$^\alpha$/H$^\alpha$ NOE correlations have been detected between the segments Pro51−Leu55 and Ala88−Pro93$_{bis}$ for nDsbD$_{C103S}$. In addition, outstandingly low S^2 values associated to τ_i or R_{ex} terms are observed for Asp53 and especially for the Ala90−Glu93 segment. This clearly proves that the high rmsd observed in these regions (see Figure 5a) are due to an actual flexibility and not to a lack of NMR restraints. It also confirms that these two segments do not display a β-strand organization in the nDsbD$_{C103S}$ structure. This could be explained by the higher global hydrophobicity of these two segments compared with their equivalents in *E. coli* nDsbD (Glu51−Ile55 and Asn88−Gly93 segments) as suggested by the electrostatic potential of both proteins (see Supporting Information, Figure S2). Indeed, in nDsbD$_{C103S}$, they contain seven nonglycine hydrophobic residues compared with four residues in *E. coli* nDsbD. Moreover, there is no such strict alternation of hydrophobic and nonhydrophobic residues in the nDsbD$_{C103}$ segments $_{52}$ADLL$_{55}$ and $_{89}$KAVG$_{92}$ as in their equivalent segments $_{52}$HAKI$_{55}$ and $_{89}$QASA$_{92}$ in *E. coli* nDsbD. Because hydrophobic residues tend to be buried in the structure, the alternation found in *E. coli* is indeed more favorable in stabilizing a β-sheet structure, with Ala53, Ile55, and Ala92 side chains on one hand and His52, Lys54, Gln89, and Ser91 side chains on the other hand pointing, respectively, inside the β-sandwich and toward the solvent. This allows, in *E. coli* nDsbD, side-chain interactions as seen between Lys54 and Gln89 or Ala53

and Ala90 and permits backbone interactions between Glu51−Ile55 and Asn88−Gly93 segments. In the case of nDsbD$_{C103S}$, Leu54 and Val91, respectively, equivalent to Lys54 and Ser91 in *E. coli* nDsbD, tend to bury their bulky side chains into the structure, to promote hydrophobic interactions, and to increase the distance between the backbone chains of the two considered segments, disabling specific β-sheet backbone interactions. Loops Ala25−Asp27, Ala88−Pro93$_{bis}$, and Phe120−Gly123 display remarkable motions at various time scales (see Figure 6). No published NMR and X-ray structures of a complex between nDsbD and tDsbD are available so far. We propose that the motions observed in this area, especially the striking flexibility of the segment Ala88−Pro93$_{bis}$, could provide adaptability to the peptidic chain to interact with tDsbD. These dynamic features may be crucial to ensure a proper contact area between the nDsbD and tDsbD domains in *Neisseria*. This hypothesis is reinforced by the noteworthy hydrophobicity and the weak electrostatic potential (see Figure 1c) of this region, which could facilitate interaction with the transmembrane domain.

To conclude, we have elucidated a solution structure of nDsbD in a reduced form and characterized its dynamics, which provides new important biological insights for the putative mechanism, so far based on crystallographic data gathered from the oxidized form or complexes. We have shown that the active site is protected by the "cap loop" between strands $\beta 6$ and $\beta 7$ both in the reduced and oxidized states. Therefore, the recognition of the two redox forms of nDsbD is not due to a conformational change of this cap loop. Moreover, a cap displacement must be triggered by the interaction with its specific partners, which can be permitted by the mobility highlighted in the Gly63−Arg73 segment and for the Gln43−Ile46 bend, forming a hinge. The results suggest a pronounced capacity of structural adjustments of the partial β-barrel upon interaction with a biological partner, whatever the reduced or oxidized forms. This could explain why nDsbD can recognize several different disulfide oxido-reductase partners. Moreover, putative recognition structural or dynamics elements in nDsbD have been proposed, not only around the active site but also in more distant regions assumed to be involved in its interaction with DsbC and tDsbD.

ACKNOWLEDGMENT

SUPPORTING INFORMATION AVAILABLE

Figure S1 showing the superimposition of the ^{1}H−^{15}N HSQC spectra of the C103S mutant (black) with the reduced form of the wild-type (green) nDsbD from *N. meningitidis*, both recorded at 600 MHz, 298 K, pH 7.0 (a), as well as the backbone amide chemical shift perturbations calculated using the consensual value $\Delta\delta$ (b), and Figure S2 corresponding to the electrostatic potential representation of *E. coli* oxidized nDsbD (a) and that of *N. meningitidis* nDsbD$_{C103S}$ (b) using two spatial orientations. This material is available free of charge via the Internet at http://pubs.acs.org.

REFERENCES

1. Stewart, E. J., Katzen, F., and Beckwith, J. (1999) Six conserved cysteines of the membrane protein DsbD are required for the transfer of electrons from the cytoplasm to the periplasm of *Escherichia coli*. *EMBO J. 18*, 5963–5971.
2. Chung, J., Chen, T., and Missiakas, D. (2000) Transfer of electrons across the cytoplasmic membrane by DsbD, a membrane protein involved in thiol-disulphide exchange and protein folding in the bacterial periplasm. *Mol. Microbiol. 35*, 1099–1109.
3. Gordon, E. H., Page, M. D., Willis, A. C., and Ferguson, S. J. (2000) *Escherichia coli* DipZ: Anatomy of a transmembrane protein disulphide reductase in which three pairs of cysteine residues, one in each of three domains, contribute differentially to function. *Mol. Microbiol. 35*, 1360–1374.
4. Goulding, C. W., Sawaya, M. R., Parseghian, A., Lim, V., Eisenberg, D., and Missiakas, D. (2002) Thiol-disulfide exchange in an immunoglobulin-like fold: structure of the N-terminal domain of DsbD. *Biochemistry 41*, 6920–6927.
5. Haebel, P. W., Goldstone, D., Katzen, F., Beckwith, J., and Metcalf, P. (2002) The disulfide bond isomerase DsbC is activated by an immunoglobulin-fold thiol oxidoreductase: Crystal structure of the DsbC-DsbDα complex. *EMBO J. 21*, 4774–4784.
6. Kim, J. H., Kim, S. J., Jeong, D. G., Son, J. H., and Ryu, S. E. (2003) Crystal structure of DsbDγ reveals the mechanism of redox potential shift and substrate specificity. *FEBS Lett. 543*, 164–169.
7. Rietsch, A., Belin, D., Martin, N., and Beckwith, J. (1996) An in vivo pathway for disulfide bond isomerization in *Escherichia coli*. *Proc. Natl. Acad. Sci. U.S.A. 93*, 13048–13053.
8. Rietsch, A., Bessette, P., Georgiou, G., and Beckwith, J. (1997) Reduction of the periplasmic disulfide bond isomerase, DsbC, occurs by passage of electrons from cytoplasmic thioredoxin. *J. Bacteriol. 179*, 6602–6608.
9. Katzen, F., and Beckwith, J. (2000) Transmembrane electron transfer by the membrane protein DsbD occurs via a disulfide bond cascade. *Cell 103*, 769–779.
10. Krupp, R., Chan, C., and Missiakas, D. (2001) DsbD-catalyzed transport of electrons across the membrane of *Escherichia coli*. *J. Biol. Chem. 276*, 3696–3701.
11. Collet, J. F., Riemer, J., Bader, M. W., and Bardwell, J. C. (2002) Reconstitution of a disulfide isomerization system. *J. Biol. Chem. 277*, 26886–26892.
12. Fabianek, R. A., Hennecke, H., Thony-Meyer, L. (1998) The active-site cysteines of the periplasmic thioredoxin-like protein CcmG of *Escherichia coli* are important but not essential for cytochrome c maturation in vivo*J. Bacteriol. 180*, 1947-1950.
13. Fabianek, R. A., Hofer, T., and Thony-Meyer, L. (1999) Characterization of the *Escherichia coli* CcmH protein reveals new insights into the redox pathway required for cytochrome c maturation. *Arch. Microbiol. 171*, 92–100.
14. Reid, E., Cole, J., and Eaves, D. J. (2001) The *Escherichia coli* CcmG protein fulfils a specific role in cytochrome c assembly. *Biochem. J. 355*, 51–58.
15. Bessette, P. H., Cotto, J. J., Gilbert, H. F., and Georgiou, G. (1999) In vivo and in vitro function of the *Escherichia coli* periplasmic cysteine oxidoreductase DsbG. *J. Biol. Chem. 274*, 7784–7792.
16. Rozhkova, A., Stirnimann, C. U., Frei, P., Grauschopf, U., Brunisholz, R., Gruetter, M. G., Capitani, G., and Glockshuber, R. (2004) Structural basis and kinetics of inter- and intramolecular disulfide exchange in the redox catalyst DsbD. *EMBO J. 23*, 1709–1719.
17. Stirnimann, C. U., Rozhkova, A., Grauschopf, U., Gruetter, M. G., Glockshuber, R., and Capitani, G. (2005) Structural basis and kinetics of DsbD-dependent cytochrome c maturation. *Structure 13*, 985–993.
18. Brot, N., Collet, J. F., Johnson, L. C., Jonsson, T. J., Weissbach, H., and Lowther, W. T. (2006) The thioredoxin domain of *Neisseria gonorrhoeae* PilB can use electrons from DsbD to reduce downstream methionine sulfoxide reductases. *J. Biol. Chem. 281*, 32668–32675.
19. Keller, R. (2004) Optimizing the process of nuclear magnetic resonance spectrum analysis and computer aided resonance assignment, Ph.D. Thesis, Swiss Federal Institute of Technology, Zurich, Switzerland.
20. Wishart, D. S., Bigam, C. G., Yao, J., Abildgaard, F., Dyson, H. J., and Oldfield, E. (1995) ^{1}H, ^{13}C and ^{15}N chemical shift referencing in biomolecular NMR. *J. Biomol. NMR 6*, 135–140.

21. Bai, Y., Milne, J. S., Mayne, L., and Englander, S. W. (1993) Primary structure effects on peptide group hydrogen exchange. *Proteins: Struct., Funct., Genet. 17*, 75–86.

22. Cordier, F., and Grzesiek, S. (2002) Temperature-dependence of protein hydrogen bond properties as studied by high-resolution NMR. *J. Mol. Biol. 317*, 39–52.

23. Cordier, F., Barfield, M., and Grzesiek, S. (2003) Direct observation of $C^{\alpha}-H^{\alpha}\cdots O=C$ hydrogen bonds in proteins by interresidue $^{h3}J_{C\alpha C'}$ scalar couplings. *J. Am. Chem. Soc. 125*, 15750–15751.

24. Herrmann, T., Güntert, P., and Wüthrich, K. (2002) Protein NMR structure determination with automated NOE-identification in the NOESY spectra using the new software ATNOS. *J. Biomol. NMR 24*, 171–189.

25. Herrmann, T., Güntert, P., and Wüthrich, K. (2002) Protein NMR structure determination with automated NOE assignment using the new software CANDID and the torsion angle dynamics algorithm DYANA. *J. Mol. Biol. 319*, 209–227.

26. Cornilescu, G., Delaglio, F., and Bax, A. (1999) Protein backbone angle restraints from searching a database for chemical shift and sequence homology. *J. Biomol. NMR 13*, 289–302.

27. Guntert, P. (2004) Automated NMR structure calculation with CYANA. *Methods Mol. Biol. 278*, 353–378.

28. Koradi, R., Billeter, M., and Wüthrich, K. (1996) MOLMOL: A program for display and analysis of macromolecular structures. *J. Mol. Graphics 14*, 51–55.

29. Farrow, N. A., Muhandiram, R., Singer, A. U., Pascal, S. M., Kay, C. M., Gish, G., Shoelson, S. E., Pawson, T., Forman-Kay, J. D., and Kay, L. E. (1994) Backbone dynamics of a free and phosphopeptide-complexed Src homology 2 domain studied by ^{15}N NMR relaxation. *Biochemistry 33*, 5984–6003.

30. Johnson, B. A., and Blevins, R. A. (1994) NMRView: A computer program for the visualization and analysis of NMR data. *J. Biomol. NMR 4*, 603–614.

31. Farrow, N. A., Zhang, O., Szabo, A., Torchia, D. A., and Kay, L. E. (1995) Spectral density function mapping using ^{15}N relaxation data exclusively. *J. Biomol. NMR 6*, 153–162.

32. Ishima, R., Yamasaki, K., Saito, M., and Nagayama, K. (1995) Spectral densities of nitrogen nuclei in *Escherichia coli* ribonuclease HI obtained by ^{15}N NMR relaxation and molecular dynamics. *J. Biomol. NMR 2*, 217–220.

33. Ishima, R., and Nagayama, K. (1995) Protein backbone dynamics revealed by quasi spectral density function analysis of amide N-15 nuclei. *Biochemistry 34*, 3162–3171.

34. Lefevre, J. F., Dayie, K. T., Peng, J. W., and Wagner, G. (1996) Internal mobility in the partially folded DNA binding and dimerization domains of GAL4: NMR analysis of the N-H spectral density functions. *Biochemistry 35*, 2674–2686.

35. Hiyama, Y., Niu, C., Silverton, J. V., Bavoso, A., and Torchia, D. A. (1988) Determination of ^{15}N chemical shift tensor via ^{15}N-^{2}H dipolar coupling in Boc-glycylglycyl[^{15}N glycine]benzyl ester. *J. Am. Chem. Soc. 110*, 2378–2383.

36. Peng, J. W., and Wagner, G. (1995) Frequency spectrum of NH bond in eglin c from spectral density mapping at multiple fields. *Biochemistry 34*, 16733–16752.

37. Dosset, P., Hus, J.-C., Blackledge, M., and Marion, D. (2000) Efficient analysis of macromolecular rotational diffusion from heteronuclear relaxation data. *J. Biomol. NMR 16*, 23–28.

38. Lipari, G., and Szabo, A. (1982) Model-free approach to the interpretation on nuclear magnetic resonance relaxation in macromolecules. 1. Theory and range of validity. *J. Am. Chem. Soc. 104*, 4546–4559.

39. Lipari, G., and Szabo, A. (1982) Model-free approach to the interpretation on nuclear magnetic resonance relaxation in macromolecules. 2. Analysis of experimental results. *J. Am. Chem. Soc. 104*, 4560–4570.

40. Quinternet, M., Selme, L., Tsan, P., Beaufils, C., Jacob, C., Boschi-Muller, S., Averlant-Petit, M.-C., Branlant, G., and Cung, M. T. (2008) ^{1}H, ^{13}C, and ^{15}N resonance assignment of the C103S mutant of the N-terminal domain of DsbD from *Neisseria meningitidis*. *Biomol. NMR Assign. 2*, 85–87.

41. Laskowski, R. A., Rullmann, J. A., MacArthur, M. W., Kaptein, R., and Thornton, J. M. (1996) AQUA and PROCHECK-NMR: Programs for checking the quality of protein structures solved by NMR. *J. Biomol. NMR 8*, 477–486.

42. Vriend, G., and Sander, C. (1993) Quality control of protein models: Directional atomic contact analysis. *J. Appl. Crystallogr. 26*, 47–60.

43. Holm, L., and Sander, C. (1993) Protein structure comparison by alignment of distance matrices. *J. Mol. Biol. 233*, 123–138.

44. Gibrat, J. F., Madej, T., and Bryant, S. H. (1996) Surprising similarities in structure comparison. *Curr. Opin. Struct. Biol. 6*, 377–385.

45. Guignard, L., Padilla, A., Mispelter, J., Yang, Y. S., Stern, M. H., Lhoste, J. M., and Roumestand, C. (2000) Backbone dynamics and solution structure refinement of the ^{15}N-labeled human oncogenic protein p13^{MTCP1}: comparison with X-ray data. *J. Biomol. NMR 17*, 215–230.

46. Constantine, K. L., Friedrichs, M. S., Goldfarb, V., Jeffrey, P. D., Sheriff, S., and Mueller, L. (1993) Characterization of the backbone dynamics of an anti-digoxin antibody VL domain by inverse detected ^{1}H-^{15}N NMR: comparisons with X-ray data for the Fab. *Proteins 15*, 290–311.

47. Stirnimann, C. U., Grütter, M. G., Glockshuber, R., and Capitani, G. (2006) nDsbD: A redox interaction hub in the *Escherichia coli* periplasm. *Cell. Mol. Life Sci. 63*, 1642–1648.

48. Gouet, P., Courcelle, E., Stuart, D. I., and Metoz, F. (1999) ESPript: Multiple sequence alignments in PostScript. *Bioinformatics 15*, 305–308.